M-band discrete wavelet transform–based deep learning algorithm for identifying thermokarst lakes in the Qinghai–Tibetan Plateau

Andrew Li[1◑*], Jiahe Liu[1◑], Olivia Liu[1◑], Xiaodi Wang[1],

1 Math Department, Western Connecticut State University, Danbury, Connecticut, United States of America

◑ These authors contributed equally to this work.

* andrew.li.application@gmail.com

Abstract

Thermokarst lakes serve as key signs of permafrost thaw, and as point sources of CH_4 in the present and near future [1]. However, detailed information on the distribution of thermokarst lakes remains sparse across the entire permafrost region on the Qinghai–Tibet Plateau (QTP). In this research, we developed a new discrete wavelet transform (DWT)–based dual-input deep learning (DL) model using a convolutional neural network (CNN) framework to automatically classify and accurately predict thermokarst lakes. We created a new 3-way tensor dataset based on raw image data from more than 500 Sentinel-2 satellite lake images and decomposed those images using state-of-the-art M-band DWTs. We also incorporated non-image feature data for various climate variables. The special data treatment adds additional features and improves validation accuracy by up to 17%. As our data pre-processing does not require any manual polygon tracing, our method is more robust and can be upscaled easily without having to collect field data.

Introduction

Background

One of the relatively recent phenomena that has been exacerbated by global warming is the accelerated thawing of permafrost triggered by rising air and ground temperatures [2]. Permafrost has historically served as the largest terrestrial carbon sink on Earth, covering approximately 24% of the northern land surface and containing around 1,600 billion tonnes of carbon, twice the amount present in the current atmosphere [3] [4]. Although the permafrost under most of the QTP region is relatively thin, it still plays a crucial role in cryospheric processes [5]. More importantly, the QTP is extremely sensitive to climate change [6]. Temperatures at elevations above 4,000 m have warmed up to 75% faster than those at elevations below 2,000 m [7]. Current climate models suggest that a considerable portion of permafrost will disappear in the coming decades [8]. The projections are supported by the effects of recent spikes in global temperatures, which have caused huge areas of permafrost to thaw, leaving behind large amounts of thermokarst terrain and releasing alarming amounts of greenhouse gases (GHGs) into the atmosphere. Therefore, increases in thermokarst features are an early indicator of increased permafrost loss and elevated GHG emissions [1]. This claim is also supported by historical evidence, as CH_4 emissions released from newly formed thermokarst lakes' bubbling comprised 33–87% of the northern latitudes' increase in atmospheric CH_4 concentration, contributing to the climate warming of past deglaciation periods [9].

Thermokarst is the most prevalent form of rapid permafrost thaw and results in thermo-erosional gullies, retrogressive thaw slumps, active layer detachment slides, thermokarst lakes, and drained thaw lake basins [10]. Thermokarst terrain appears in northern latitudes where permafrost has collapsed, leading to relatively high levels of diffusion and ebullition of GHGs, particularly CH_4 [1]. Diffusion and ebullition are two pathways of GHG release from the water into the atmosphere. Ebullition refers to fluxes of CH_4 bubbles or gas pockets from sediments and water columns [11]. Of the different types of thermokarst terrain, thermokarst lakes contribute the most to CH_4 emissions, with expected emissions of 4.1 ± 2.2 Tg of CH_4 per year, or roughly 17–26% of the total emissions from all northern lakes; by 2300, the total projected permafrost carbon feedback could reach up to 0.39 ℃ [1].

Seasonal fluctuations of emissions have been observed. Certain lakes, including floating ice lakes, contain CH_4 trapped in ice bubbles during the winter months, causing peak seasonal emissions in the warmer months [1]. Despite these observations, long-term CH_4 emissions from thermokarst lakes are still a highly uncertain bottleneck preventing the scientific community from fully discerning the global CH_4 budget [12]. To remedy these uncertainties, our research aims to distinguish thermokarst lakes from non-thermokarst lakes.

There exist major distinctions between non-thermokarst permafrost lakes and thermokarst lakes. First, thermokarst lakes must form above rapidly thawing ice-rich permafrost, providing an impermeable foundation that prevents immediate water drainage [13]. Currently, thermokarst lakes cover approximately 7% of total permafrost-affected land [14]. Most thermokarst lakes in the QTP region, in particular, form on top of continuous permafrost [15]. A meaningful feature of permafrost is the active layer thickness (ALT), which is a layer of soil that freezes and thaws annually. The thermokarst process is catalyzed by the deepening of the active layer; different disruptions, including temperature warming, can trigger this process, causing subsequent subsidence or erosion. The extent of a resulting depression may depend on the elevation and shape of the terrain. The expansion of thermokarst lakes is accelerated by heat conduction, which leads to thawing of water bodies below and around the thermokarst region [1]. Taliks, layers of unfrozen ground, begin to form under these lakes. They facilitate one way of rapid thawing beneath the lakes, causing vertical expansion [16]. The development of non-thermokarst lakes occurs independently of this process.

Another distinctive feature of thermokarst lakes is their water content. Much of the water that forms thermokarst lakes can be attributed to the melted ice within the thawed permafrost. Organic matter from melted permafrost is decomposed by microbes [13]. This matter is highly reactive and releases more nutrients than soil, creating a positive feedback loop that encourages additional activity, which generates more GHG emissions [1]. This decomposition of organic matter is dependent on oxygen availability: a high availability of oxygen leads to the production of CO_2 gas, while low availability leads to the production of CH_4 gas [1].

As water drains, the thermokarst process decelerates, and vegetation growth amplifies [13]. Identifying thermokarst lakes serves as a prerequisite for predicting drainage events that shape the surface landscape, catalyzing large-scale changes in topography and carbon cycling [2]. Further, they can introduce significant quantities of sediment and nutrients to nearby water bodies, altering the ecosystems of the lakes and rivers [8]. For example, past LiDAR satellite imagery has exposed linear corrugations, deep thermo-erosional gullies, and drainage channels [17]. Thermokarst lakes can also disrupt the regular pattern of soil temperature fluctuations; they have the ability to raise sediment temperatures by up to 10℃ above the mean annual air temperature [18].

Related works

Other studies have explored the classification of thermokarst landforms. A plethora of semiautomatic methods to predict land cover have incorporated machine learning (ML) techniques into their model frameworks, including k-means clustering, random forest regression, maximum likelihood classifiers, and DL models such as TempCNN [2] [6] [16] [15] [19]. However, these models maintain a manual component in either the post-processing or training stages. Most image-based classification models solely utilize the 3 RGB channels and a few additional infrared light channels. The two indices based on the infrared channels most frequently used to map surface water bodies are the Normalized Difference Water Index (NDWI) and the Modified Normalized Difference Water Index (MNDWI) [6]. Although the NDWI is a cost-efficient and time-efficient method of extracting water surface information, solely basing classification off the NDWI can risk underclassifying lakes above a certain depth, as shallow lakes are less likely to reflect the green spectral channel and do not absorb the near-infrared light to the same extent.

More extensive pre-processing has yet to be applied to classifying thermokarst landforms. Some studies have omitted all additional data pre-processing [20] [16] [19]. The few studies that had used Sentinel data that had performed data pre-processing only utilized the Sentinel Application Platform (SNAP) [21] [15]. These studies do not take full advantage of the potential of pre-processing. To our knowledge, SNAP only covers visualization, resampling, and mosaic operations [22]. More advanced pre-processing techniques, such as DWTs, have the power to unlock hidden information stored in satellite images, as well as to enhance resolution to improve model accuracy [23]. We hope to expand wavelet decomposition applications to this field by decomposing the Sentinel-2 data. We chose to use Sentinel-2 data rather than satellite imagery from other sources, such as Landsat, because it is the highest resolution available and captures images at high frequency.

Over the past few years, DL has found applications in permafrost research, from predicting thermokarst landslide susceptibility [19], to mapping retrogressive thaw slumps [24], to mapping lake ice in Canada [25]. We found only two studies that took advantage of CNNs to identify thermokarst lakes [2]. [16] utilizes a temporal CNN (TempCNN) to automatically map floating lake ice and explore the temporal dynamics of ice changes. However, because the authors chose only to employ the temporal dimension, the classification model remained one-dimensional [25]. The second study investigates the applicability of DL to classifying retrogressive thaw slumps (RTS). Other studies employed DeepLab for the purpose of semantic segmentation [2]. For our research objectives, using semantic segmentation would not be ideal, as differences between the details of individual pixels of thermokarst and non-thermokarst lakes may not be as distinctive or noticeable. Classification would be much more difficult, as feature extraction would be significantly limited.

Although some model frameworks have used advanced ML models to extract exact boundaries of thermokarst lakes, their investigations into smaller thermokarst lakes is poorly resolved. Many studies were unable to include lakes with surface areas less than $0.4\,\mathrm{km}^2$ in their evaluation, leaving these smaller water bodies severely underdocumented [26]. However, in the Arctic circle, small thermokarst lakes were found to be the most active CH_4 generators [27]. Given this information, it can reasonably be assumed that the surface area is not strongly correlated with the activity of GHG emissions, and the omission of smaller lakes could lead to large underestimations of water body surface area and CH_4 emissions.

The objectives of this study were: (1) to assess the capability of dual input CNN in classifying thermokarst lakes from high-resolution satellite imagery and non-image feature data; (2) to improve the model accuracy by integrating M-band DWTs that decompose each of our raw data images into M^2 different sub-images with different frequencies to form a new corresponding 3-way tensor dataset; and (3) to classify smaller thermokarst lakes previously excluded from similar studies.

We created a new 3-way tensor dataset based on raw image data for more than 500 Sentinel-2 satellite lake images and decomposed those images using state-of-the-art M-band DWTs. We also incorporated non-image feature data for various climate variables. These methods significantly improved our model's performance.

A illustration of our model framework is shown in Fig 1.

Fig 1. Model Framework.

Materials and methods

Advantages of machine learning

Modern ML algorithms have found applications in almost every field. The most significant advantage of DL methods, in particular, is that they can automatically learn features [28]. Traditional supervised models require users to input a number of variables that they believe would produce an optimal model. Unsupervised models removes the expertise and knowledge barrier [2]. CNNs are the most popular ML method used for remote sensing image classification, as they perform better at spatial feature extraction [29]. Our model based on wavelet decomposed data paired with a CNN serves as a huge improvement over previous attempts to integrate ML into thermokarst identification. Not only is our model fully automated to allow for ease of scaling up, but it is also one of the first to integrate over fifteen non-image feature datasets including air and ground temperature, precipitation, and snow depth. However, because a portion of the model is a black box, it is difficult to outline exactly which features and channels were analyzed, as the weights and biases of the CNN nodes can only reveal preliminary information about their influences.

Being able to identify and analyze the distribution of thermokarst lakes is essential for understanding the full extent of thermokarst influence on long-term release of CO_2 and CH_4 stocks, on geomorphological processes, vegetation and peat dynamics, to ultimately improve current predictive tools to manage climate change.

Study area

In this research, we studied the entire QTP region bounded by longitudes 67–104° E and latitudes 27–46° N. Nicknamed the Roof of the World and the Third Pole, the QTP is the highest and largest plateau on Earth with an average elevation of 4,400 m and an area of approximately 2.5×10^6 km^2. Precipitation in the QTP is usually the heaviest between June and September, and the mean annual air temperature is 6.0 °C [19] [30]. These conditions form a typical alpine vegetation ecosystem. Recent vegetation maps suggest that alpine environments can be classified into alpine steppes, alpine swamp meadows, alpine meadows, and alpine deserts [30]. Snow cover in the QTP functions as the main source of fresh water in western China and all major Asian rivers [31]. These major rivers, including the Yangtze River, the Yellow River, and the Brahmaputra River, provide water to about 1.4 billion people downstream [32]. Therefore, the formation and disappearance of thermokarst lakes in the QTP can significantly affect the water balances in surrounding regions. The QTP also happens to be the largest high-altitude and low-latitude permafrost zone, where up to 53% of exposed land is underlain by permafrost [32]. The permafrost in this region is particularly susceptible to global warming because of its relatively high ground temperatures, with averages above −3.0 °C [19].

Data collection

Lake selection and distribution

We began our methodology workflow by constructing our own lake image datasets. We determined our ground truth labels using a preexisting 2020 thermokarst lake inventory from [15] and a preexisting 2018 glacial lake inventory from [33]. The glacial lake inventory was selected to avoid overlap of lakes. Furthermore, glacial lakes are of similar size as thermokarst lakes, which means that they may be more difficult to distinguish using other methods [15]. These inventories provided coordinates for 114,420 thermokarst lakes and 30,121 and glacial lakes respectively. Although the glacial lake inventory was taken in 2018, a glacial lake cannot transform into a thermokarst lake. Thus, we can reasonably assume lakes that the locations of glacial and non-thermokarst lakes in 2018 remain representative of glacial and non-thermokarst lakes in 2020, provided that the lake did not drain or disappear during those two years.

We removed glacial lakes from the Altay and Sayan region from our dataset due to excessive distance from the study area (Fig 2A). There were 4,677 lakes in this area, or around 16% of the entire inventory (Fig 2B).

We then filtered our data to only select lakes with surface areas between $0.2\,\mathrm{km}^2$ and $0.5\,\mathrm{km}^2$. These steps reduced our datasets to 1,030 thermokarst lakes and 1,015 glacial lakes (Fig 2C). From there, we extracted around a quarter of the available lakes in each of the two datasets (Fig 2D).

Fig 2. Distribution of thermokarst and glacial Lakes. (A) Distribution of glacial lakes. Lakes in the Altay and Sayan region are in green, and lakes not in that region are in blue. The lakes in the Altay and Sayan region are clearly outside the QTP and are far from the other glacial lakes. There are also lakes in the High Asia region outside the QTP included in this inventory. (B) Distribution of thermokarst (yellow) and glacial lakes (blue) that meet our location criteria. (C) Distribution of thermokarst and glacial lakes that meet our location and size criteria. (D) Distribution of sample thermokarst and glacial lakes that are used in our model. The sample lakes we selected have a similar spatial distribution as the population of lakes meeting our size criteria, which also has a similar spatial distribution as the population of all lakes in the inventories.

Image data

As both lake inventories contained coordinates of the centers of every lake, we were able to extract satellite data for a certain bounding box around each lake, centered at each lake's centroid.

For each lake in our lake collection, we obtained image data for the $1{,}440\,\mathrm{m} \times 1{,}440\,\mathrm{m}$ area around it. Because the spatial resolution of our image data was $10\,\mathrm{m} \times 10\,\mathrm{m}$, our extracted images of each lake contained 144×144 pixels. Due to the range of lake sizes, certain entries in our dataset contained multiple lakes within the given 144×144 pixels.

We used the red, green, blue, near-infrared (NIR), short-wave infrared 1 (SWIR 1) and short-wave infrared 2 (SWIR 2) channels of the Level-2A (Bottom of Atmosphere reflectance) product using high-resolution satellite imagery from the Sentinel-2 MSI. This data was downloaded using the Google Earth Engine API, using Google Earth Engine's `COPERNICUS/S2_SR` product.

Along with these 6 channels, we added 3 spectral indices: the NDWI, the NDVI, and the Brightness Index (BI). These indices were calculated using the following formulas [15]:

$$\mathrm{NDWI} = \frac{G - \mathrm{NIR}}{G + \mathrm{NIR}} \tag{1}$$

$$\mathrm{NDVI} = \frac{R - \mathrm{NIR}}{R + \mathrm{NIR}} \tag{2}$$

$$\mathrm{BI} = \sqrt{\frac{C_R R + C_G G}{2}} \tag{3}$$

Here, C_R and C_G are constants. They have been set to 1 for the purposes of this study.

These three indices can help highlight characteristics of water, vegetation, and soil, respectively. The NDWI and the NDVI can assist with mapping surface water bodies [34].

The NDWI is used to delineate and enhance water features while ignoring soil and vegetation features; it functions on the notion that water bodies reflect minimally in the green channel and also produce lower radiation in the NIR channel [35].

The NDVI reflects the density of chlorophyll pigments found in plant matter and vegetation [6]. It can thus be used to measure vegetation development [36].

The BI captures the characteristics of the soil. It is related to the brightness of the soil and, therefore, is influenced by factors such as soil moisture and organic matter on the soil surface [37].

Because some satellite images were obscured by clouds, we manually selected non-cloudy images from each lake's collection of images between August 1, 2020 and October 1, 2020. To avoid biases and ensure a random, representative sample, we first shuffled the lake inventories before manually selecting from them. Each satellite image from the time range was displayed, and we manually selected images where the lake was not blocked by clouds. If we could not find a good picture for a lake, we skipped it entirely. This could skew our data to contain fewer lakes in more cloudy areas, as we removed 47 thermokarst lakes and 45 glacial lakes, approximately 18.3% of the lakes we looked at in total. However, we believe our sample is still representative because most important variables have similar distributions in our sample as in the population; we discussed this in detail in the section "Representativeness of our sample".

Fig 3. An example of the manual selection process. The thumbnail images are scenes from multiple days between August and September 2020. Images 2, 6, 7, 8, 10, and 12 are optimal for selection, and we would select one of them for our training data.

In total, we selected 252 thermokarst lakes and 251 glacial lakes, which comprised both our training and validation datasets.

Fig 4 shows some examples of glacial and thermokarst lakes. The figure shows a diversity of lakes, and it is not necessarily easy to visually determine which lakes are of which type.

Fig 4. Sample thermokarst and glacial lake images. (A) Thermokarst lakes. (B) Glacial lakes.

Non-image climate data

We incorporated the monthly averaged ERA5-Land dataset from the Copernicus Climate Data Store to supplement our image inputs [38]. This dataset is composed of monthly averages of the hourly ERA5-Land dataset.

The spatial resolution of this data is $0.1^\circ \times 0.1^\circ$, or approximately $81\,\text{km}^2$. Because of the limited resolution of the ERA5-Land dataset, we assign a single data point of variable values to each lake, i.e., the values for the pixel that each lake center falls in. Due to monthly weather data variability between August and September 2020, our final input values for each lake represent the mean of the value between the two months.

Table 1 lists out each variable we used and a description of each variable.

Variable name	Description
2-meter air temperature (K)	Air temperature at 2 m above ground
Evaporation (m of water equivalent)	The amount of water that has evaporated
Evaporation from bare soil (m of water equivalent)	Amount of evaporation from bare soil
Lake bottom temperature (K)	Temperature of water at the bottom of water bodies
Lake ice surface temperature (K)	Temperature of the top surface of ice on water bodies
Lake ice total depth (m)	Thickness of ice on water
Lake shape factor (dimensionless)	Describes the way that temperature changes with depth / shape of the vertical temperature profile
High vegetation leaf area index (m^2m^{-2})	Surface area of one side of all the leaves found over an area of land for vegetation classified as 'high'
Low vegetation leaf area index (m^2m^{-2})	Surface area of one side of all the leaves found over an area of land for vegetation classified as 'low'
Snow albedo (0–1)	Measure of the reflectivity of snow-covered parts of grid box
Snow cover (%)	Percentage of snow-covered areas of grid box
Snow depth (m)	Depth of snow
Snow evaporation (m of water equivalent)	Amount of water evaporation from snow
Snowmelt (m of water equivalent)	Accumulated amount of water that has melted from snow in snow-covered area of grid box.
Soil temperature level 1 (K)	The temperature of the soil at 0–7 cm.
Surface runoff (m)	Water from rainfall or melting snow that does not get stored in the soil and instead drains away over the surface.
Total precipitation (m)	The accumulated liquid and frozen water that falls to the Earth's surface; sum of large-scale precipitation and convective precipitation.

Table 1. Non-image variables we used and their descriptions

While no single variable is enough to distinguish between classes of lakes, a lake possessing an outlier value for one or more variables can strongly suggest which class it belongs to. Thus, these variables can help provide additional insight for the model. Variables such as lake bottom temperature, snowmelt, and soil temperature have intuitive reasons why they should help the most in distinguishing between lake classes the most because their distributions may differ between the two classes of lakes. We verify this intuition in a subsection of discussion section (Section) by confirming that these three variables are the ones our model uses the most.

Data pre-processing

M-Band DWT

An orthogonal M-band DWT was used to decompose each channel of our images into M^2 different frequency channels, components, or subimages. DWTs can be useful to obtain some hidden information of an image by separating low-frequency from high-frequency parts. An M-band DWT is determined by a filter bank consisting of M filters ($M \geq 2$), including a low-pass filter α and $M-1$ high-pass filters $\beta^{(j)}$ for $j = 1, \ldots, M-1$.

An M-band wavelet filter bank is said to have N vanishing moments if its filters satisfy the following conditions [39]:

$$\sum_{i=1}^{n} \alpha_i = \sqrt{M} \tag{4}$$

$$\sum_{i=1}^{n} i^k \beta_i^{(j)} = 0 \qquad \text{for } k = 0, \ldots, N-1,\ j = 1, \ldots, M-1 \tag{5}$$

$$\|\alpha\| = \|\beta^{(j)}\| = 1 \qquad \text{for } j = 1, \ldots, M-1 \tag{6}$$

$$\langle \alpha, \beta^{(j)} \rangle = 0 \qquad \text{for } j = 1, \ldots, M-1 \tag{7}$$

$$\langle \beta^{(i)}, \beta^{(j)} \rangle = 0 \qquad \text{for } i, j = 1, \ldots, M-1 \text{ and } i \neq j \tag{8}$$

A wavelet is said to be N-regular if it has N vanishing moments. Intuitively, wavelets with more vanishing moments tend to be smoother and have longer filters.

For sufficiently large integer values of k, an M-band wavelet can be used to create an $Mk \times Mk$ wavelet transform matrix used to decompose channels of that dimension.

It can be proven that all the DWT matrices we are using are orthogonal, i.e., $W^{\mathrm{T}} = W^{-1}$ for all such DWT matrices W.

The 2D DWT of an channel X is defined as the matrix WXW^{T}. This decomposition can be seen as an $M \times M$ block matrix where the top-left submatrix is the approximation (low frequency) component, and the other submatrices are detail (high frequency) components.

For example, a 2D 3-band DWT decomposes a channel X into a block matrix

$$WXW^{\mathrm{T}} = \begin{bmatrix} A & D_{12} & D_{13} \\ D_{21} & D_{22} & D_{23} \\ D_{31} & D_{32} & D_{33} \end{bmatrix}$$

where A is the approximation, or low frequency, component and D_{ij} are detail, or high frequency, components.

To pre-process our data, we used the Daubechies wavelets Daubechies-6 and Daubechies-8, along with a 3-band 2-regular wavelet, a 4-band 2-regular wavelet, and a 4-band 4-regular wavelet. The filter banks of the 3- and 4-band wavelets can be found in Section in the Appendix.

Because the dimensions of a wavelet transform matrix are divisible by the band of the wavelet, we chose to make our image resolution divisible by 12, since we are using 2-, 3-, and 4-band wavelets. Fig 5A is a 144 × 144 pixel image of a thermokarst lake. Because our image data have multiple channels, we applied DWTs to decompose each channel separately. Using the 3-band 2-regular wavelet in the Appendix, it is decomposed into approximation and detail components. Each component is a 48 × 48 pixel image. The approximation component is shown in Fig 5B. Te detail component is shown in Fig 5C with the approximation component in top left corner. Because we applied a 3-band DWT to the image, the image is decomposed into 9 sub-images (components or channels). The pixel values of detail components are very small compared to that of the approximation component.

The detail component with scaled color in shown in Fig 5D. It is the same as the full result but with the RGB values multiplied by 64. It can be seen that the detail components directly to the right of or below the approximation component show horizontal or vertical detail, respectively. The other detail components are various diagonal detail components.

Fig 5. Thermokarst lake before and after wavelet transformation (A) Original image of thermokarst lake. (B) Approximation component of wavelet decomposition using the 3-band 2-regular wavelet. (C) The full result of wavelet decomposition using the 3-band 2-regular wavelet. (D) The full result of wavelet decomposition using the 3-band 2-regular wavelet with scaled color.

Representativeness of our sample

We performed a t-test to determine whether our samples were representative of our populations. The t-tests' null hypotheses are that the samples' and the populations' values have equal expected values, and their alternate hypotheses were that the variables' values have distinct expected values. Our t-test was an independent t-test; we used Welch's t-test.

In Table 2, lake ice surface temperature and lake ice total depth had no p-values because their standard deviations are zero, suggesting that none of the thermokarst lakes had ice on their surfaces. For both the population dataset and sample dataset of thermokarst lakes, none of the lakes had corresponding lake ice temperatures above the freezing point of 273 K or 0 ℃. so the standard deviation was 0, resulting in undefined p-values.

Variable	p-value
Surface runoff	0.00
Total precipitation	0.00
Snow albedo	0.00
2 meter temperature	0.00
Soil temperature level 1	0.01
Leaf area index, high vegetation	0.01
Snowmelt	0.05
Leaf area index, low vegetation	0.06
Snow cover	0.07
Snow depth	0.07
Snow evaporation	0.11
Lake bottom temperature	0.25
Evaporation from bare soil	0.38
Evaporation	0.53
Lake shape factor	0.63
Lake ice surface temperature	N/A
Lake ice total depth	N/A

Table 2. p-values for thermokarst lakes. Suface runoff, total precipitation, snow albedo, 2 meter temperature, soil temperature level 1, and high vegetation leaf area index all produced statistically significant p-values. We explore their distributions and explain these results later in this section.

In Table 3, however, lake ice surface temperature and lake ice total depth had definable p-values. This difference is understandable, as analyzing the glacial lake ice depth distributions show that approximately 9% of glacial lakes in both the sample and population had nonzero lake ice depth labels and subsequently lake ice temperatures below 273 K; 93 glacial lakes in the population and 26 glacial lakes in the sample

Variable	p-value
Surface runoff	0.07
Total precipitation	0.07
Snowmelt	0.14
Evaporation from bare soil	0.33
Lake shape factor	0.34
Snow evaporation	0.46
Lake ice surface temperature	0.46
Evaporation	0.51
Snow cover	0.55
Snow depth	0.62
Lake ice total depth	0.63
2 metre temperature	0.66
Lake bottom temperature	0.74
Snow albedo	0.91
Leaf area index, high vegetation	0.93
Leaf area index, low vegetation	0.93
Soil temperature level 1	0.98

Table 3. p-values for glacial lakes. None of these values are significant, indicating that our sample is representative of our population.

dataset had nonzero lake depth values. Similarly, 93 glacial lakes in the population dataset and 24 glacial lakes in the sample dataset had lake ice temperatures below the freezing point of 273 K or 0 °C.

S1 Fig. shows that for all of the features that failed the t-test, their sample distributions are very similar, if not nearly identical, to their corresponding population variable value distributions. The most notable difference in the distributions that were not identical is a greater number of upper extreme values in each feature's population distribution. For some features, such as surface runoff and total precipitation, these extremes heavily increased the maximum values in their respective distributions. This observation indicates that none of the distributions were normal or close to normal, providing an additional reason why a ML model is preferable to a traditional regression-based model.

While we did not input the latitude, longitude, lake area, and elevation variable values into our model, we performed a two-tailed independent means t-test on the population and sample means of these two variables for both glacial and thermokarst lakes to further assess the representativeness of our sample dataset. The p-values for thermokarst lakes are shown in in Table 4. The p-values for glacial lakes are shown in in Table 5. While the p-values for elevation and latitude are significant for thermokarst lakes, plotting the histograms of the distributions reveals that the distributions are in fact also very similar (S2 Fig.). A potential explanation as to why the data produced such small p-values is that neither distribution fits the normal curve. Both distributions are left skewed.

Variable	p-value
Elevation	0.01
Latitude	0.01
Longitude	0.16
Area	0.95

Table 4. p-values for thermokarst lakes. The p-values for elevation and latitude are significant.

Variable	p-value
Latitude	0.05
Longitude	0.21
Elevation	0.28
Area	0.50

Table 5. p-values for glacial lakes. None of the p-values are significant.

Model framework

S3 Fig. shows the flowchart of our classification model combining image data input and non-image feature data into a CNN.

Training and testing

Given a completed model framework and data pre-processing methodology, we were able to create seven different models to test how our framework would respond to seven different types of input data. First, we split our dataset into training and validation datasets using sklearn's train_test_split, we divided our datasets into a 70–30 training-to-testing ratio: 70% of our data was used to train our model while the remaining 30% was used to test our model and validate the performance of our model. Note that a random state parameter was utilized to ensure that the data were divided with identical seeds for each model (i.e.,each model's testing and training datasets contained identical data points).

Then, we developed seven models to be trained that corresponded to seven different modifications of our datasets. This included a true control in which we trained one model exclusively on the non-decomposed image dataset, a dual input control in which we trained one model on the non-decomposed image dataset and the non-image feature dataset, and five experimental models in which we tested the effects of five DWTs with distinctive filter banks on our data: Daubechies-6 (db3), Daubechies-8 (db4), a 3-band 2-regular wavelet (wv32), a 4-band 2-regular wavelet (wv42), and a 4-band 4-regular wavelet (wv44). Certain DWTs produced unique spatial tensor shapes, necessitating modifications of certain parameters to better match each set of required learning objectives. The model parameters in question include the input dimension, kernel size of each convolutional layer, and number of strides in each average pooling layer. They can be found in Table 6, which summarizes the specific alterations made to each model.

	Image Data?	Non-Image Data?	DWT?	Input Dimensions	Kernel Size	Strides
True control	✓	✗	✗	$144 \times 144 \times 9$	(9, 9)	3
Dual input control	✓	✓	✗	$144 \times 144 \times 9$	(9, 9)	3
Daubechies-6 (db3)	✓	✓	✓	$72 \times 72 \times 36$	(9, 9)	3
Daubechies-8 (db4)	✓	✓	✓	$72 \times 72 \times 36$	(9, 9)	3
3-band 2-regular (wv32)	✓	✓	✓	$48 \times 48 \times 81$	(5, 5)	2
4-band 2-regular (wv42)	✓	✓	✓	$36 \times 36 \times 144$	(5, 5)	2
4-band 4-regular (wv44)	✓	✓	✓	$36 \times 36 \times 144$	(5, 5)	2

Table 6. A summary of the seven types of input data we trained our model on.

Results

After training our model, we tested its classification performance on our validation dataset and recorded each model's confusion matrix and receiver operating characteristics (ROC) curve. Table 7 summarizes our findings for the seven models. Note that because glacial lakes had a label of 0 and thermokarst lakes had a label of 1, the confusion matrices should be read as (starting from the upper left corner and moving clockwise) true negatives, false positives, true positives, false negatives.

Summary of metrics

The area under an ROC curve is a measurement of how well a model is able to distinguish between two classes; generally, ROC curves that resemble right angles in the top left indicate better performance. Our 4-band 2-regular DWT model performed the

	Accuracy	Precision	Recall	F1 Score	Area Under ROC Curve
True control	0.7219	0.6739	0.8533	0.7529	0.81
Dual input control	0.7748	0.7204	**0.8933**	0.7976	0.82
Daubechies-6 (db3)	0.8212	0.8077	0.8400	0.8235	0.87
Daubechies-8 (db4)	0.8146	0.7701	**0.8933**	0.8272	0.86
3-band 2-regular (wv32)	0.8212	0.8077	0.8400	0.8235	0.85
4-band 2-regular (wv42)	**0.8940**	**0.9403**	0.8400	**0.8873**	**0.94**
4-band 4-regular (wv44)	0.8344	0.8378	0.8267	0.8322	0.89

Table 7. A table summary of five metrics of evaluation calculated based on each model's testing performance. The highest values in each category are in bold.

best under this metric, with the highest area under the ROC curve (Fig 6 A). Unsurprisingly, our true control model performed the worst(Fig 6 C), scoring the lowest in every metric we measured but recall. The dual input control model produced a significantly better confusion matrix, but its ROC curve showed very little improvement over the true control, suggesting that despite having an additional 17 non-image features, the dual input control's ability to distinguish between thermokarst and glacial lakes did not improve significantly.

In Fig 6B confusion matrix of the model using the 4-band 2-regular (wv42) DWT, there is a very low number of false positives and a medium number of false negatives. In Fig 6D confusion matrix of the true control model with the input of image-only non–wavelet-decomposed satellite data, there are significantly more (31) false positives than false negatives (11).

In S4B Fig. confusion matrix of the dual input control model using non-wavelet decomposed data, the amount of false negatives is low (8), while the amount of false positives is much higher (26). In S4D Fig. Confusion matrix of the model using the Daubechies-6 (db3) DWT, the recorded number of false positives and false negatives are very similar. In S4F Fig. confusion matrix of the model using the Daubechies-8 (db4) DWT, there is a low number of false negatives. The number of false positives is moderately high, but lower than in the dual input control model. S5B Fig. confusion matrix of the model using the 3-band 2-regular (wv32) DWT is the same as the confusion matrix for the Daubechies-6 DWT. In S5D Fig. confusion matrix of the model using the 4-band 4-regular (wv44) DWT, the amounts of false positives and false negatives are very similar and neither low nor high.

The use of DWTs greatly improved the classification capabilities of the remaining

Fig 6. ROC curves and confusion matrices for 4-band 2-regular model vs. true control. (A) The ROC curve of the selected model using the 4-band 2-regular (wv42) DWT. (B) The confusion matrix of the selected model using the 4-band 2-regular (wv42) DWT. (C) The ROC curve of the true control model with the input of image-only non–wavelet-decomposed satellite data. (D) The confusion matrix of the true control model with the input of image-only non–wavelet-decomposed satellite data.

five models. By splitting each channel in our image data into approximation and detail channels, we were able to effectively generate more features and uncover potentially hidden information that the models could use to distinguish between thermokarst and glacial lakes. The 4-band 2-regular decomposition had the greatest positive impact on the performance of the model, producing an accuracy of almost 90% and an area under the ROC curve of 0.94, demonstrating that the model was able to effectively distinguish between thermokarst and glacial lakes.

The 4-band 2-regular DWT likely produced such positive results for two reasons. First, 4-band DWT divides each image into the highest number of detail channels, giving our model the most features to train from. More bands should generally produce better results, and this is suggested by the fact that as the number of bands in the DWT method increased, its corresponding model's performance in all five metrics generally increased. Second, the 2-regular aspect of this DWT entails that it produced detail channels (components) that were less smooth than the 4-band 4-regular counterpart. This is significant because the images in our dataset were relatively lower-resolution (144×144); each channel was rough, in that the variation in values from pixel to pixel was greater. The smooth 4-regular DWT would have negatively impacted the quality of the resulting channels.

Our model, trained on the 4-band 2-regular DWT decomposed spatial data and normalized non-image feature data, produced a very high precision of 0.9043 but a relatively lower recall of 0.8400. This indicates that the model produced far fewer false positives than false negatives.

To test which parts of the 4-band 2-regular DWT decomposed data were the most important for our model, we first obtained the weights of our model's first convolutional layer as an array with shape $9 \times 9 \times 144 \times 9$. We then split the array along axis 2 to isolate the weights of each layer and calculated the average weight value of each layer. We found no significant pattern that would suggest that the model tended to assign more weight to a specific decomposed set of channels. However, we found that the nine layers with the lowest average weights corresponded to the nine approximation channel (channels 0 to 8). To further test this theory, we randomly shuffled the approximation channels of our testing dataset to create noise that would be effectively useless in the model's classification. Then, we tested our model with a dataset that used those noisy channels to see the result. Our model saw a 5% decrease in accuracy, but its area under the ROC curve only decreased by 0.02, suggesting that while the noise might have disturbed the model's ability to classify certain lakes, it generally had very little impact on the model's ability to distinguish between thermokarst and glacial lakes. These experiments suggested that the model trained on 4-band 2-regular DWT decomposed data relied more heavily on detail channels than approximation channels when classifying between thermokarst and glacial lakes. This result is consistent with our observation that training our model on 4-band 2-regular DWT decomposed data, the less smooth data, yielded better results than the model trained on 4-band 4-regular DWT decomposed data.

Discussion

We designed an automatic dual input classification model based on DL to identify thermokarst lakes in the QTP region from high-resolution satellite imagery and additional non-image feature data. We explored the application of M-band DWTs to pre-process our image data and produce expanded features. Scenes between August and September 2020 were obtained from Sentinel-2 satellite image datasets. We based our ground truths labels on two separate inventories of thermokarst and glacial lake inventories. We extracted 252 thermokarst lakes and 251 glacial lakes from the respective inventories. We obtained climate feature data from the ERA5-Land Monthly Averaged dataset. To ensure that our sample of thermokarst and glacial lakes were representative of all of the lakes that met our area criteria, we performed multiple two independent means two-tailed t-tests on each of our population and sample means of our non-image climate feature data and additional features. A CNN was then trained and tested using our normalized and DWT-processed data to output a classification of either thermokarst or non-thermokarst.

In addition to successfully producing a relatively high accuracy classification model of thermokarst lakes based on a CNN, the hypotheses that a) incorporating wavelet transforms to decompose our image data into 3-way tensor image data and b) combining image data and non-image climate data would increase accuracy was supported. The use of non-image data and 2D DWTs greatly increased the accuracy of the model by 17.21%.

When evaluating model accuracy, it is important to consider whether the greatest increase in accuracy was caused by the additional non-image feature data input or the pre-processing using the wavelet transforms. Although both amendments improved model accuracy compared to the true control, the wavelet decomposition impacted the model performance the most, increasing accuracy by up to 11.9% and F1 score by up to 0.09. Comparing the dual input control to the true control, we can see that the addition of the second non-image climate feature data input affected the model's performance slightly less; it increased accuracy by up to 5.29% and increased the F1 score by up to 0.045.

Exploration the significance of feature variables

The following section explores the 3 climate feature variables with the greatest average absolute weights in the first Dense layer of our 4-band 2-regular DWT model. We compare and analyze the distributions of lake bottom temperature, snowmelt, and soil temperature level 1 of thermokarst lakes and glacial lakes.

The mean lake bottom temperature for thermokarst lakes is higher than that of the glacial lakes. Some of thermokarst lake bottoms are somewhat warmer (282–284 K) than most glacial lakes. This observation is logical, as microbes usually decompose thawed organic matter at anoxic lake bottoms. This is correlated with higher temperatures and additional permafrost thaw in a positive feedback loop [13] [40] (Fig 7A).

While thermokarst lakes' snowmelt values are all very close to zero, glacial lakes sometimes have higher snowmelt values, reflecting the fact that glacial lakes must be in or near glacial regions, which are more likely to have snow (Fig 7B).

Glacial lakes more often have lower soil temperatures, including below freezing point (273.15 K). This could be due to glacial lakes in glacial regions being colder (Fig 7C).

Fig 7. Significance of feature variables: lake bottom temperature, snowmelt, and level 1 soil temperature (A) Lake bottom temperature for thermokarst and glacial lakes. (B) Snowmelt for thermokarst and glacial lakes. (C) Level 1 soil temperature for thermokarst and glacial lakes.

Applications

We believe that the results obtained are significant enough for our model to be used in accurately creating annual inventories of thermokarst lakes, without the need for field data. Because the study area in our investigation was significantly larger, the applications expand beyond regional or local analysis. Given the fact that our image and non-image data sources have global coverage, our model should be applicable to any region with a meaningful amount of thermokarst lakes. This would greatly reduce the cost of tracking thermokarst lakes, as the need for field equipment and research centers would be nullified.

A broader application of annual thermokarst lake inventories would be to increase precision in both global climate models and GHG budgets. Identification of thermokarst landforms is a prerequisite to understanding their GHG outputs in more detail. Thermokarst lakes are the most significant thermokarst landform. By identifying their location, it may be possible to discern their contributions to annual CO_2 and CH_4 emissions, thus informing more accurate simulations of the Earth's climate.

Future work

With the simultaneous progression of ML techniques and quality of satellite and remote sensing imagery, the future possibilities of deep learning to further improving classification, automatic mapping, and forecasting of thermokarst landforms exceeds those covered in this research.

First, to improve the time efficiency of our data collection process, a script should be developed to automatically select the image with the least cloud cover and cloud shadows of the extracted satellite image options. We would be able to construct a relatively accurate thermokarst lake inventory for any time period with sufficient high-resolution satellite image data. We were unable to accomplish this step because the cloud coverage area property on the satellite image dataset was unreliable due to the scale of the data. We had also attempted to combine multiple images from the same location by selecting pixels with the median channel values together; however, the results remained inconsistent. Potential ways to overcome this problem could be improvements in the quality and accuracy of satellite image parameters or innovative ways to work around cloud cover via deeper exploration into band value correlation with percentage of cloud cover.

Another option for expanding our training dataset would be to include land as a possible classification. By doing so, it would be possible to automatically detect new or previously-undiscovered thermokarst lakes by running the model on images from randomly-chosen locations.

As introduced in the Related Works, a few other studies have applied time series CNNs (TempCNN) to mapping thermokarst landforms [25]. Future research could explore a potential ensemble or hybrid model that combines our model with that of TempCNN so that it would be plausible to input time-series data. This addition could also provide more information and expand on research related to investigating the dynamics and seasonal changes of thermokarst lakes.

In this research, we were able to classify and include relatively smaller lakes, but there are still water bodies with smaller surface areas that we were unable to include due to limitations in our data resolution. Because the input images had to remain constant in size, including smaller lakes would sacrifice resolution, as the pixel representation of the lake would be insignificant compared to the land cover in the bounding box.

Building on our classification of lakes, our next step would be forecasting certain surface dynamics of thermokarst lakes, such as change in surface area or drainage prediction. These predictions would be based off our dual input time-series image data and non-image feature data. Our current limitation is the resolution of our non-image climate data. The highest resolution dataset that includes the features we hope to include is of 9 km horizontal resolution. This would grossly generalize the feature data of thermokarst regions with that of surrounding land, which could potentially include other thermokarst or non-thermokarst water bodies that would not be accounted for.

Conclusion

In this research, we explore the degradation of permafrost in the QTP region through the classification of thermokarst lakes and develop a DWT-based dual input DL model with a CNN to automatically classify and accurately predict thermokarst lakes with area between 0.2 and 0.5 km^2, a range of lakes previously excluded from many assessments due to issues in satellite data. Our model is the first neural network–based thermokarst lake classification model that incorporates M-band DWTs to decompose raw spatial data into M^2 different frequency component sub-images to form a corresponding 3-way tensor dataset. This special treatment of our data adds additional features and improves validation accuracy by up to 17%. Our model can be upscaled and used to build future inventories of thermokarst lakes without having to collect field data.

Supporting information

S1 Appendix. Filter banks for the 3- and 4-band wavelet transforms. Tables 8, 9, and 10 contain filter banks for the 3- and 4-band wavelet transforms we used.

α	$\beta^{(1)}$	$\beta^{(2)}$
0.33838609728386	−0.11737701613483	0.40363686892892
0.53083618701374	0.54433105395181	−0.62853936105471
0.72328627674361	−0.01870574735313	0.46060475252131
0.23896417190576	−0.69911956479289	−0.40363686892892
0.04651408217589	−0.13608276348796	−0.07856742013185
−0.14593600755399	0.42695403781698	0.24650202866523

Table 8. Filter bank for the 3-band 2-regular wavelet.

α	$\beta^{(1)}$	$\beta^{(2)}$	$\beta^{(3)}$
−0.067371764	−0.094195111	−0.094195111	−0.067371764
0.094195111	0.067371764	−0.067371764	−0.094195111
0.40580489	0.567371764	0.567371764	0.40580489
0.567371764	0.40580489	−0.40580489	−0.567371764
0.567371764	−0.40580489	−0.40580489	0.567371764
0.40580489	−0.567371764	0.567371764	−0.40580489
0.094195111	−0.067371764	−0.067371764	0.094195111
−0.067371764	0.094195111	−0.094195111	0.067371764

Table 9. Filter bank for the 4-band 2-regular wavelet.

α	$\beta^{(1)}$	$\beta^{(2)}$	$\beta^{(3)}$
0.08571302	−0.1045086525	0.2560950163	0.1839986022
0.1931394393	0.1183282069	−0.2048089157	−0.662289313
0.3491805097	−0.1011065044	−0.250343323	0.6880085746
0.5616494215	−0.0115563891	−0.2484277272	−0.1379502447
0.4955029828	0.6005913823	0.4477496752	0.0446493766
0.4145647737	−0.2550401616	0.0010274	−0.0823301969
0.2190308939	−0.4264277361	−0.0621881917	−0.0923899104
−0.1145361261	−0.082739818	0.5562313118	−0.0233349758
−0.0952930728	0.0722022649	−0.2245618041	0.0290655661
−0.1306948909	0.2684936992	−0.3300536827	0.0702950474
−0.0827496793	0.1691549718	−0.2088643503	0.0443561794
0.0719795354	−0.443703932	0.220295183	−0.0918374833
0.0140770701	0.0849964877	0.0207171125	0.0128845052
0.0229906779	0.1388163056	0.0338351983	0.0210429802
0.0145382757	0.0877812188	0.0213958651	0.0133066389
−0.0190928308	−0.1152813433	−0.0280987676	−0.0174753464

Table 10. Filter bank for the 4-band 4-regular wavelet.

S2 Appendix. Code. The code not present in this paper can be found in this GitHub repository: `https://github.com/jliu2006/pingo`.

S1 Fig. Distributions of the non-image climate feature values that failed the t-test ($p \leq 0.05$) for thermokarst lakes. The histograms in each subfigure summarize the distribution for our sample of 252 thermokarst lakes, while the histograms below in each subfigure represent the distribution for our population of 1,030 thermokarst lakes that met our area criteria. A: Surface runoff. B: Total precipitation. C: Snow albedo. D: 2 m temperature. E: Soil temperature level 1. F: Leaf area index, high vegetation.

S2 Fig. Elevation and latitude of the sample and population of thermokarst lakes. (A) Elevation distribution. (B) Latitude distribution. The distributions are both very similar.

S3 Fig. Flowchart of our classification model.

S4 Fig. ROC curves and confusion matrices for non-selected models using no wavelets or Daubechies wavelets (A) The ROC curve of the dual input control model using non–wavelet decomposed data. (B) The confusion matrix of the dual input control model using non–wavelet decomposed data. (C) ROC curve of the model using the Daubechies-6 (db3) DWT. (D) The confusion matrix of the model using the Daubechies-6 (db3) DWT. (E) The ROC curve of the model using the Daubechies-8 (db4) DWT. (F) The confusion matrix of the model using the Daubechies-8 (db4) DWT.

S5 Fig. The ROC curves and confusion matrices for non-selected models using non-Daubechies wavelets. (A) The ROC curve of the model using the 3-band 2-regular (wv32) DWT. (B) The confusion matrix of the model using the 3-band 2-regular (wv32) DWT. (C) The ROC curve of of the model using the 4-band 4-regular (wv44) DWT. (D) The confusion matrix of of the model using the 4-band 4-regular (wv44) DWT.

Acknowledgments

First, we thank Western Connecticut State University for providing its facilities in which we conducted our research.

We are grateful for Vincent Li's mentorship on this project. He provided valuable insight into the intricacies of the model framework, assisted us with our questions on the neural network, and regularly reviewed our progress.

We are also grateful for Tyler Wooldridge's mentorship in furthering our understanding of the possible model structures and extent of ML, helping us steer our project in the right direction.

We appreciate the advice and ML expertise of Hieu Nguyen, who helped answer our inquiries and challenges we faced whilst designing our classification model.

Author Contributions

Conceptualization: Xiaodi Wang, Olivia Liu, Andrew Li, Jiahe Liu

Data curation: Andrew Li

Formal analysis: Andrew Li, Jiahe Liu

Writing — original draft preparation: Olivia Liu, Andrew Li, Jiahe Liu

Writing — review & editing: Xiaodi Wang, Andrew Li, Jiahe Liu, Olivia Liu

References

1. Zandt MHi, Liebner S, Welte CU. Roles of Thermokarst Lakes in a Warming World. Cell Press. 2020;28(10):769–779. doi:https://doi.org/10.1016/j.tim.2020.04.002.

2. Huang L, Liu L, Jiang L, Zhang T. Automatic Mapping of Thermokarst Landforms from Remote Sensing Images Using Deep Learning: A Case Study in the Northeastern Tibetan Plateau. Remote Sensing. 2018;10(12). doi:10.3390/rs10122067.

3. Grosse G, Jones B, Arp C. 8.21 Thermokarst Lakes, Drainage, and Drained Basins. In: Shroder JF, editor. Treatise on Geomorphology. San Diego: Academic Press; 2013. p. 325–353. Available from: https://www.sciencedirect.com/science/article/pii/B9780123747396002165.

4. Jin H, Ma Q. Impacts of Permafrost Degradation on Carbon Stocks and Emissions under a Warming Climate: A Review. Atmosphere. 2021;12(11):1425.

5. Gao T, Zhang Y, Kang S, Abbott BW, Wang X, Zhang T, et al. Accelerating permafrost collapse on the eastern Tibetan Plateau. Environmental Research Letters. 2021;16(5):054023.

6. Șerban RD, Jin H, Șerban M, Luo D, Wang Q, Jin X, et al. Mapping thermokarst lakes and ponds across permafrost landscapes in the Headwater Area of Yellow River on northeastern Qinghai-Tibet Plateau. International Journal of Remote Sensing. 2020;41(18):7042–7067.

7. Remington R. Climate Change Affecting High-Altitude Regions at Faster Rate, Rutgers Study Finds; 2015. Available from: https://www.rutgers.edu/news/climate-change-affecting-high-altitude-regions-faster-rate-rutgers-study-

8. Bowden WB. Climate change in the Arctic–permafrost, thermokarst, and why they matter to the non-Arctic world. Geography compass. 2010;4(10):1553–1566.

9. Walter K, Edwards M, Grosse G, Zimov S, Chapin III F. Thermokarst lakes as a source of atmospheric CH4 during the last deglaciation. science. 2007;318(5850):633–636.

10. Wei Z, Du Z, Wang L, Zhong W, Lin J, Xu Q, et al. Sedimentary organic carbon storage of thermokarst lakes and ponds across Tibetan permafrost region. Science of The Total Environment. 2022;831:154761.

11. Zamanpour MK, Kaliappan RS, Rockne KJ. Gas ebullition from petroleum hydrocarbons in aquatic sediments: A review. Journal of Environmental Management. 2020;271:110997. doi:https://doi.org/10.1016/j.jenvman.2020.110997.

12. Sieczko AK, Duc NT, Schenk J, Pajala G, Rudberg D, Sawakuchi HO, et al. Diel variability of methane emissions from lakes. Proceedings of the National Academy of Sciences. 2020;117(35):21488–21494.

13. Anthony K, Zimov S, Grosse G, Jones MC, Anthony P, FS III C, et al. A shift of thermokarst lakes from carbon sources to sinks during the Holocene epoch. Nature. 2014;511(7510):452–456.

14. Serikova S, Pokrovsky OS, Laudon H, Krickov IV, Lim AG, Manasypov RM, et al. High carbon emissions from thermokarst lakes of Western Siberia. Nature Communications. 2019;10(1552). doi:https://doi.org/10.1038/s41467-019-09592-1.

15. Wei Z, Du Z, Wang L, Lin J, Feng Y, Xu Q, et al. Sentinel-Based Inventory of Thermokarst Lakes and Ponds Across Permafrost Landscapes on the Qinghai-Tibet Plateau. Earth and Space Science. 2021;8(11):e2021EA001950. doi:https://doi.org/10.1029/2021EA001950.

16. Shaposhnikova M, Duguay CR, Roy-Léveillée. Bedfast and Floating Ice Dynamics of Thermokarst Lakes Using a Temporal Deep Learning Mapping Approach: Case Study of the Old Crow Flats, Yukon, Canada. EGUsphere. 2022;2022:1–36. doi:10.5194/egusphere-2022-388.

17. Edwards ME, Grosse G, Jones B, Mcdowell P. The evolution of a thermokarst-lake landscape: Late Quaternary permafrost degradation and stabilization in interior Alaska. Sedimentary Geology. 2016;340. doi:10.1016/j.sedgeo.2016.01.018.

18. Hughes-Allen L, Bouchard F, Laurion I, Séjourné A, Marlin C, Hatté C, et al. Seasonal patterns in greenhouse gas emissions from thermokarst lakes in Central Yakutia (Eastern Siberia). Limnology and Oceanography. 2021;66:S98–S116.

19. Yin G, Luo J, Niu F, Lin Z, Liu M. Machine learning-based thermokarst landslide susceptibility modeling across the permafrost region on the Qinghai-Tibet Plateau. Landslides. 2021;18(7):2639–2649.

20. Chen H, Liqiang T, Zhaocheng G, Jienan T, Hua W, Peng H. A Dynamics Trend Analysis Method of Thermokarst Lakes Based on the Machine Learning Algorithm. In: 2021 IEEE International Geoscience and Remote Sensing Symposium IGARSS. IEEE; 2021. p. 6484–6487.

21. Șerban RD, Jin H, Șerban M, Luo D. Shrinking thermokarst lakes and ponds on the northeastern Qinghai-Tibet plateau over the past three decades. Permafrost and Periglacial Processes. 2021;32(4):601–617. doi:https://doi.org/10.1002/ppp.2127.

22. Gunasekaran A. Tutorial in SNAP Desktop for Sentinel 2 Data Pre Processing Applications -GNU GPL Environment; 2020.

23. Rathod M, Khanapuri J. Performance Evaluation of Transform Domain Methods for Satellite Image Resolution Enhancement. In: Vasudevan H, Deshmukh AA, Ray KP, editors. Proceedings of International Conference on Wireless Communication. Singapore: Springer Singapore; 2018. p. 227–236.

24. Huang L, Luo J, Lin Z, Niu F, Liu L. Using deep learning to map retrogressive thaw slumps in the Beiluhe region (Tibetan Plateau) from CubeSat images. Remote Sensing of Environment. 2020;237:111534.

25. Shaposhnikova, Maria. Temporal Deep Learning Approach to Bedfast and Floating Thermokarst Lake Ice Mapping using SAR imagery: Old Crow Flats, Yukon, Canada; 2021. Available from: `http://hdl.handle.net/10012/17414`.

26. Chen X, Mu C, Jia L, Li Z, Fan C, Mu M, et al. High-resolution Dataset of Thermokarst Lakes on the Qinghai-Tibetan Plateau. Earth System Science Data Discussions. 2020;2021:1–23. doi:https://doi.org/10.5194/essd-2020-378.

27. Polishchuk Y V Polischchuk. The System of Geo-Simulation Modeling of Thermokarst Lakes Fields Based on the Log-Normal Distribution of Their Sizes. Advances in Intelligent Systems Research. 2020;174:195–199. doi:DOI:10.2991/aisr.k.201029.037.

28. LeCun Y, Bengio Y, Hinton G. Deep learning. nature. 2015;521(7553):436–444.

29. Ma L, Liu Y, Zhang X, Ye Y, Yin G, Johnson BA. Deep learning in remote sensing applications: A meta-analysis and review. ISPRS journal of photogrammetry and remote sensing. 2019;152:166–177.

30. Wang X, Yu C, Peng D, Gonsamo A, Liu Z. Snow cover phenology affects alpine vegetation growth dynamics on the Tibetan Plateau: Satellite observed evidence, impacts of different biomes, and climate drivers. Agricultural and Forest Meteorology. 2018;256:61–74. doi:https://doi.org/10.1016/j.agrformet.2018.03.004.

31. Luo J, Niu F, Lin Z, Liu M, Yin G. Thermokarst lake changes between 1969 and 2010 in the beilu river basin, qinghai–tibet plateau, China. Science Bulletin. 2015;60(5):556–564.

32. Cao B, Zhang T, Wu Q, Sheng Y, Zhao L, Zou D. Permafrost zonation index map and statistics over the Qinghai–Tibet Plateau based on field evidence. Permafrost and Periglacial Processes. 2019;30(3):178–194.

33. Wang X, Guo X, Yang C, Liu Q, Wei J, Zhang Y, et al. Glacial lake inventory of high-mountain Asia in 1990 and 2018 derived from Landsat images. Earth System Science Data. 2020;12(3):2169–2182. doi:10.5194/essd-12-2169-2020.

34. Qiao B, Zhu L, Yang R. Temporal-spatial differences in lake water storage changes and their links to climate change throughout the Tibetan Plateau. Remote Sensing of Environment. 2019;222:232–243.

35. McFeeters SK. The use of the Normalized Difference Water Index (NDWI) in the delineation of open water features. International Journal of Remote Sensing. 1996;17(7):1425–1432. doi:10.1080/01431169608948714.

36. Dorigo W, de Jeu R, Chung D, Parinussa R, Liu Y, Wagner W, et al. Evaluating global trends (1988–2010) in harmonized multi-satellite surface soil moisture. Geophysical Research Letters. 2012;39(18). doi:https://doi.org/10.1029/2012GL052988.

37. Marques MJ, Alvarez A, Carral P, Sastre B, Bienes R. The use of remote sensing to detect the consequences of erosion in gypsiferous soils. International Soil and Water Conservation Research. 2020;8(4):383–392. doi:https://doi.org/10.1016/j.iswcr.2020.10.001.

38. Muñoz Sabater J. ERA5-Land monthly averaged data from 1981 to present; 2019.

39. Liu Z, Liu T, Sun W, Zhao Y, Wang X. M-Band Wavelet-Based Imputation of scRNA-seq Matrix and Multi-view Clustering of Cells. The FASEB Journal. 2022;36(S1). doi:https://doi.org/10.1096/fasebj.2022.36.S1.R5102.

40. Zimov SA, Voropaev YV, Semiletov IP, Davidov SP, S F Prosiannikov FSCI, Chapin MC, et al. North Siberian Lakes: A Methane Source Fueled by Pleistocene Carbon. Science. 1997;277(5327):800–802. doi:DOI: 10.1126/science.277.5327.800.

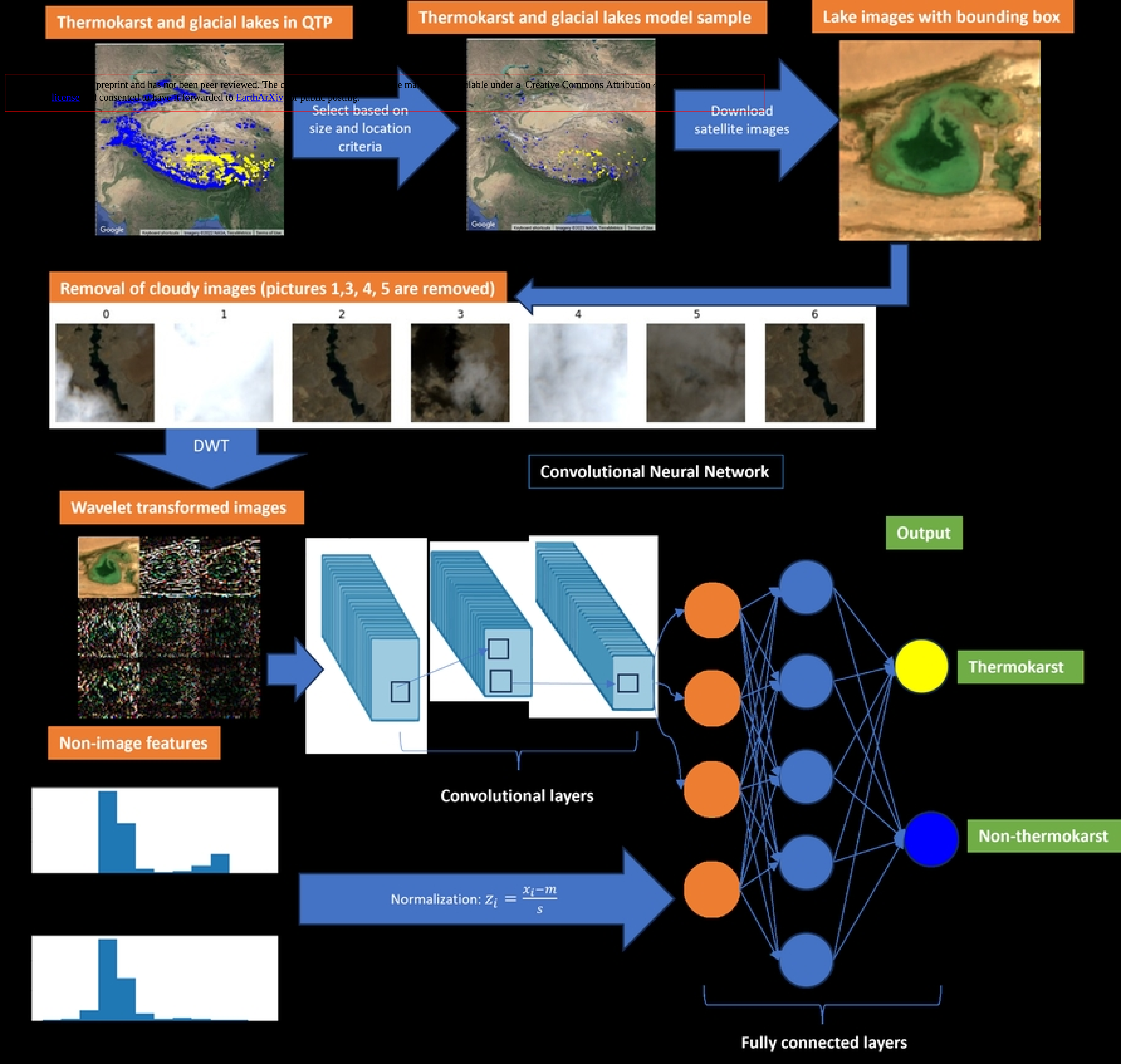
Thermokarst and glacial lakes in QTP
Select based on size and location criteria
Thermokarst and glacial lakes model sample
Download satellite images
Lake images with bounding box
Removal of cloudy images (pictures 1,3, 4, 5 are removed)
0
1
2
3
4
5
6
DWT
Wavelet transformed images
Convolutional Neural Network
Output
Thermokarst
Non-thermokarst
Non-image features
Convolutional layers
Normalization: $z_i = \frac{x_i - m}{s}$
Fully connected layers
Google

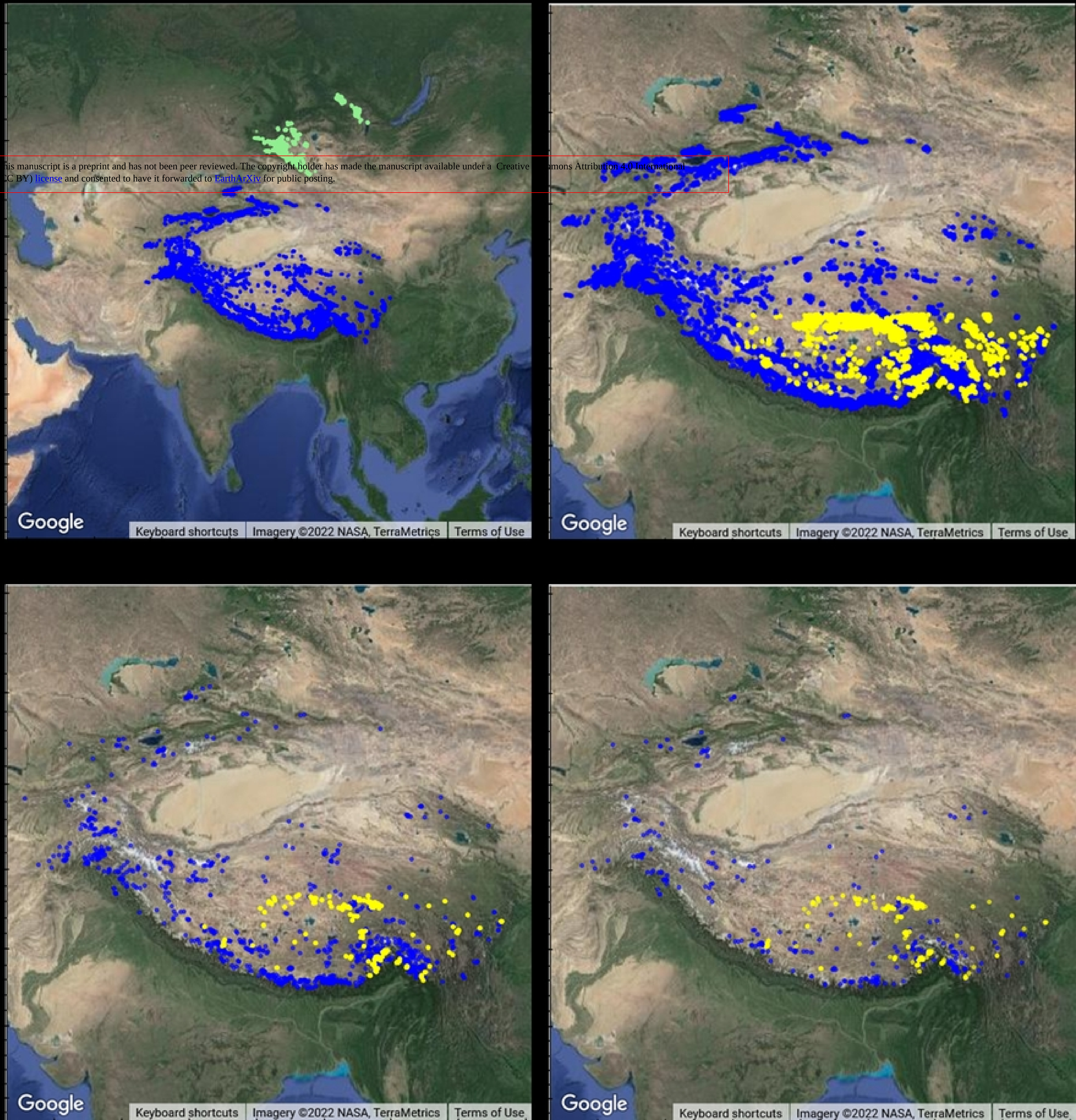
Google
Keyboard shortcuts
Imagery ©2022 NASA, TerraMetrics
Terms of Use
Google
Keyboard shortcuts
Imagery ©2022 NASA, TerraMetrics
Terms of Use
Google
Keyboard shortcuts
Imagery ©2022 NASA, TerraMetrics
Terms of Use
Google
Keyboard shortcuts
Imagery ©2022 NASA, TerraMetrics
Terms of Use

Found a total of 13 images at scale 10

0	time	datetime	B4	B3	B2
0	1596259229016	2020-08-01 05:20:29.016	1	70	162
1	1596691232113	2020-08-06 05:20:32.113	10264	10616	11192
2	1597123229552	2020-08-11 05:20:29.552	38	193	284
3	1597555231996	2020-08-16 05:20:31.996	2868	2916	2698
4	1597987229677	2020-08-21 05:20:29.677	7896	8280	8680
5	1598419231470	2020-08-26 05:20:31.470	2722	2740	2570
6	1598851229351	2020-08-31 05:20:29.351	1	194	130
7	1599283227552	2020-09-05 05:20:27.552	1	200	140
8	1599715228578	2020-09-10 05:20:28.578	59	324	296
9	1600147230427	2020-09-15 05:20:30.427	2198	2216	1958
10	1600579228129	2020-09-20 05:20:28.129	149	512	496
11	1601011231435	2020-09-25 05:20:31.435	3140	3062	3038
12	1601443229265	2020-09-30 05:20:29.265	1	389	372

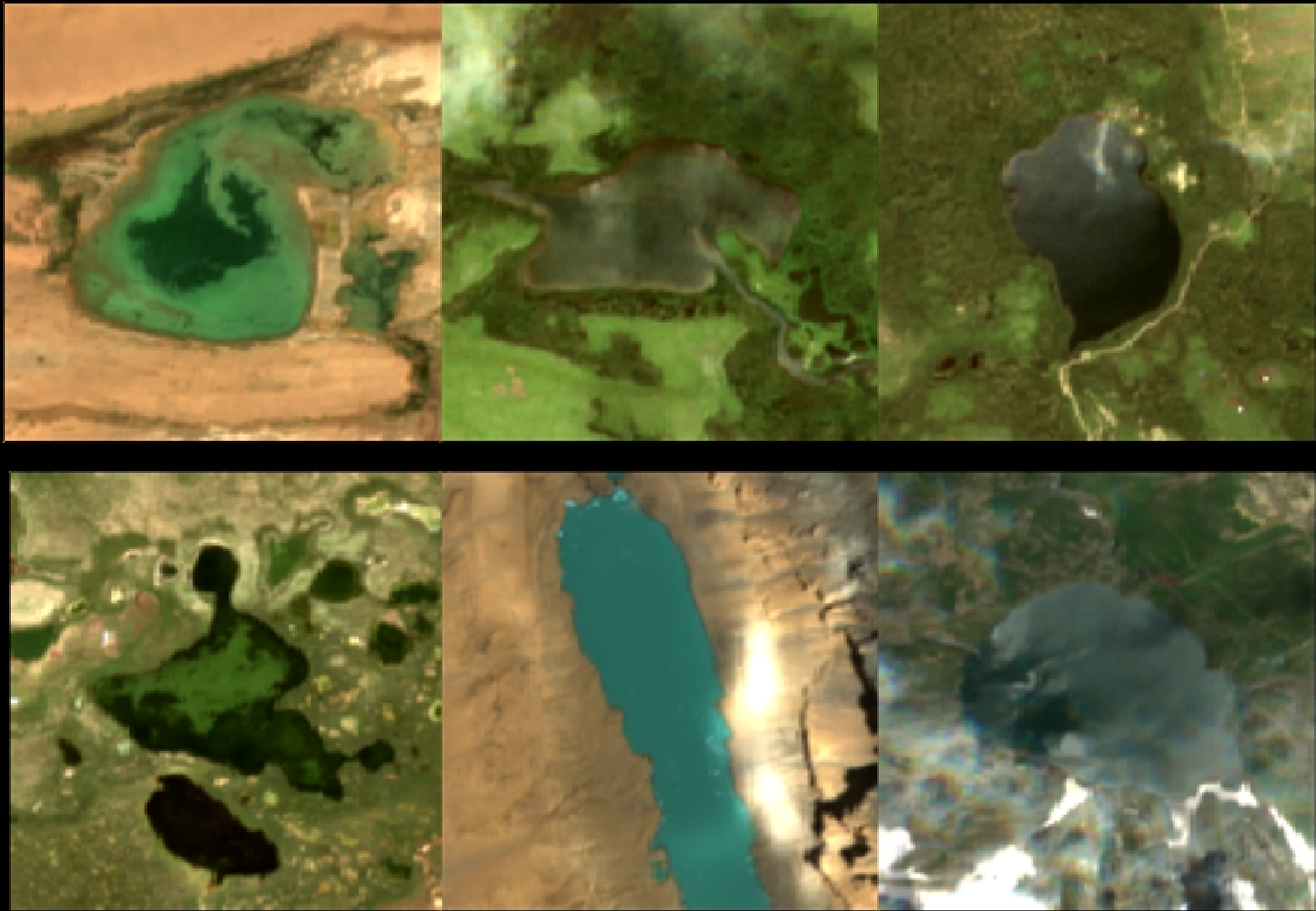

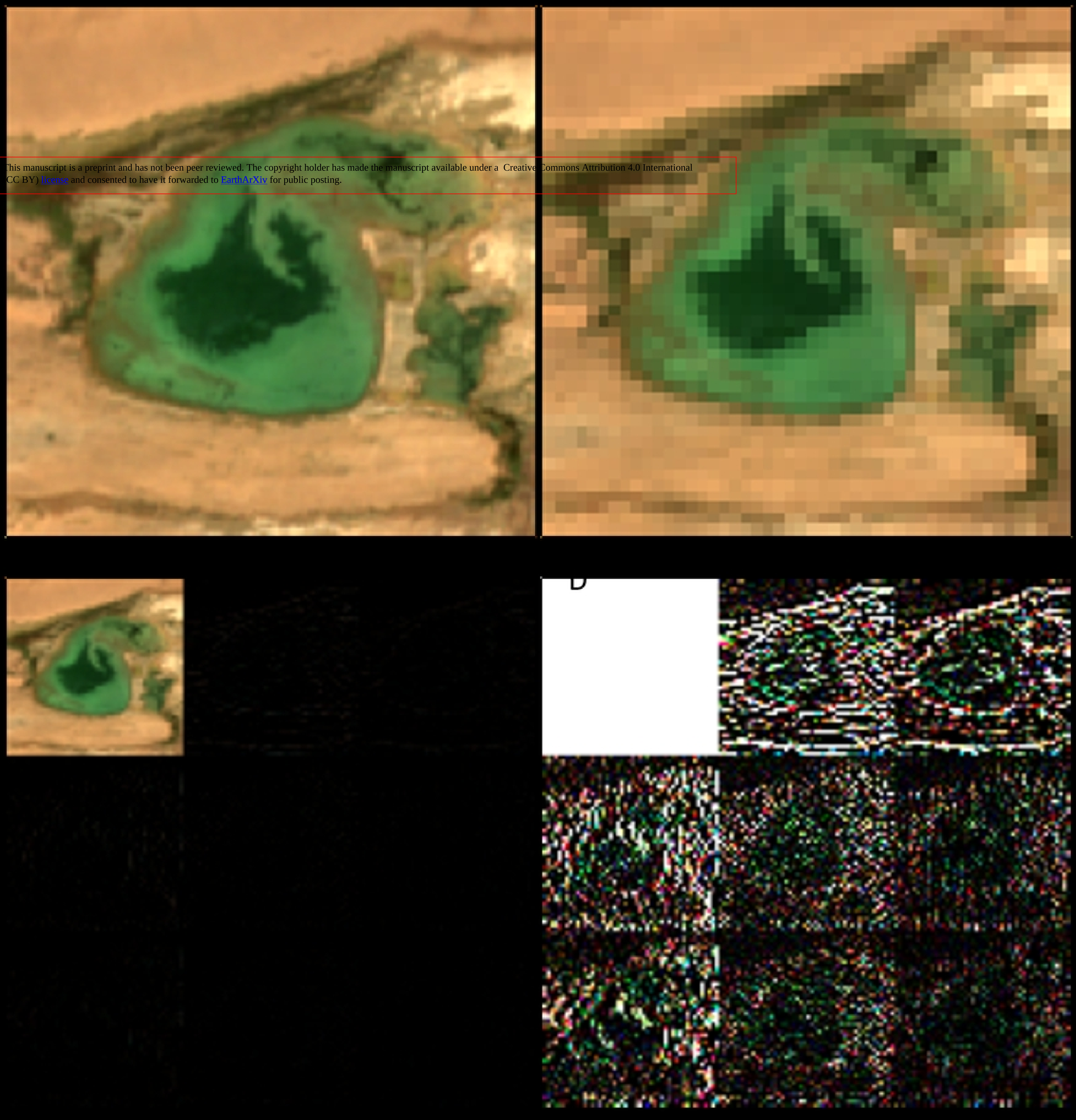

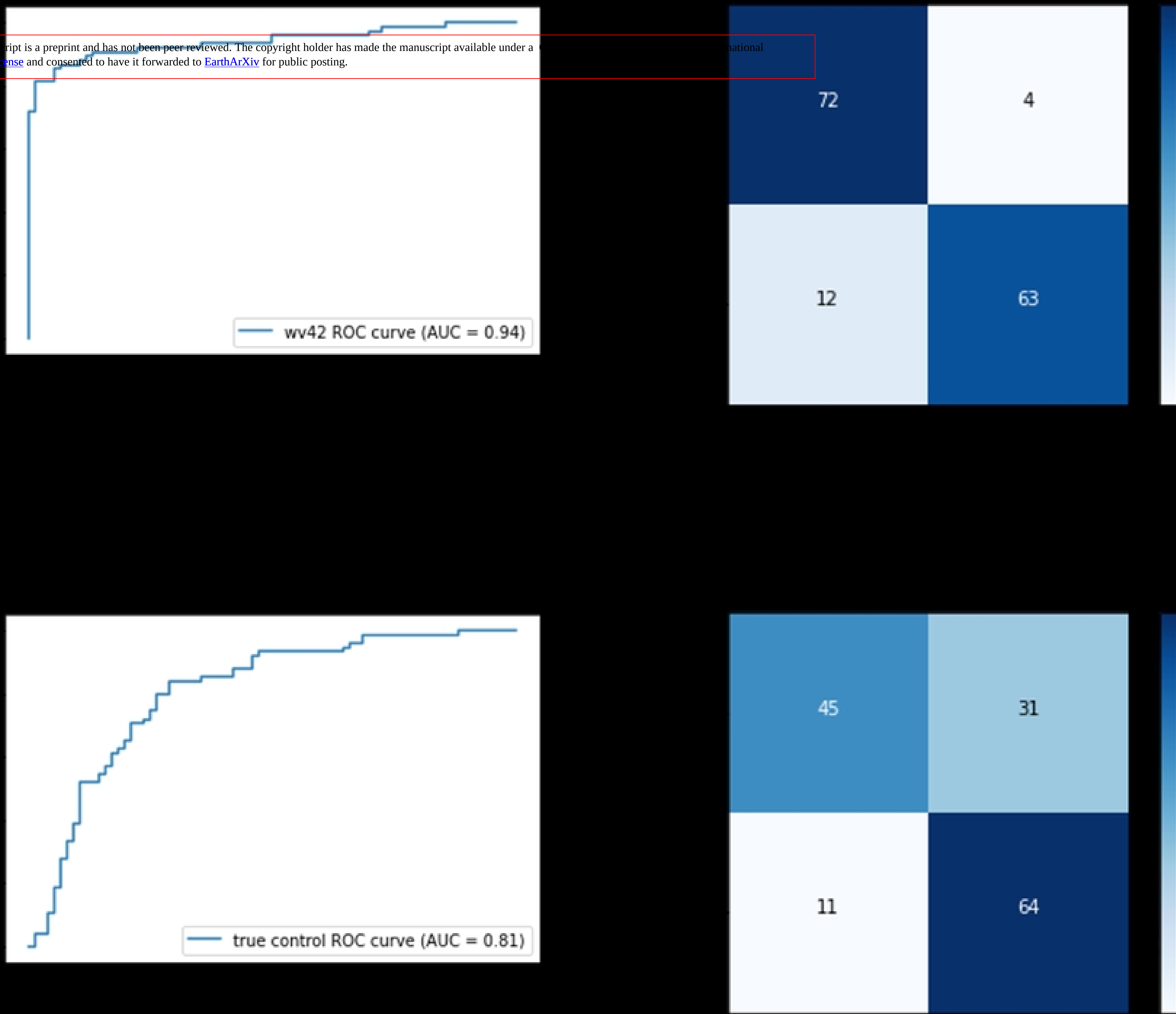
wv42 ROC curve (AUC = 0.94)
72
4
12
63
true control ROC curve (AUC = 0.81)
45
31
11
64